Maxwell-dilaton dynamics

Steven L. Liebling⬤

Department of Physics, Long Island University, Brookville, New York 11548, USA

The dynamics of the Maxwell-dilaton theory in Minkowski spacetime are studied using fully nonlinear, numerical evolutions. This model represents the flat-space sector of the Einstein-Maxwell-dilaton theory which has attracted interest recently because it is a well-posed alternative to general relativity, and it also represents the Abelian sector of the Yang-Mills-dilaton. As such, understanding its dynamics may shed light on the dynamics of the respective larger systems. In particular, we study electric, magnetic, and dyonic monopoles as well as the flux tubes studied previously by Gibbons and Wells. Some scenarios produce large gradients that an increasing adaptive mesh refinement fails to resolve. This behavior is suggestive, although far from conclusive, that the growth leads to singularity formation. No sharp transition between singularity formation and either dispersion or stationarity is found, unlike other nonlinear systems that have demonstrated a behavior similar to the black hole critical behavior at such transitions.

I. INTRODUCTION

The Maxwell-dilaton system contains an electromagnetic field coupled nonminimally to a scalar field. The dilaton acts as something of a scalar, attractive "gravity" allowing for compact solutions such as those found by Morris [1] and Gibbons and Wells [2].

This system also represents a particular sector of the more general Einstein-Yang-Mills-dilaton model. The model studied here results from restricting to flat-space and the U(1) Abelian gauge field [3]. If one instead allows for curved space, one has the Einstein-Maxwell-dilaton model studied recently [4–12]. Understanding the dynamics of this simpler system may help elucidate aspects of the more general system.

This nonlinear system is also interesting in its own right. The monopole and flux tube solutions, as found by Gibbons and Wells [2], can be used as initial data to study their stability properties. The instability found in the fully relativistic model of Ref. [4], because its analysis relied on the equation of motion for the dilaton without relying on a particular form for the metric, is expected to remain in this restricted model. Some nonlinear systems have demonstrated a type of critical behavior similar to that found in gravitational scalar collapse [13], such as Refs. [14–19], and so we look for such threshold behavior here. Most of the behavior observed has been spherical and the hope with this model is that such behavior at the threshold may be less symmetric since the dynamics of vacuum Maxwell only occurs outside spherical symmetry.

II. EQUATIONS OF MOTION

We begin by varying the appropriate action in flatspace,

$$S = \int d^4x [a_0(\partial\phi)^2 + a_1 e^{-2\kappa\phi}F_{ab}F^{ab}], \quad (1)$$

where ϕ is the dilaton, F^{ab} is the Faraday tensor for the electromagnetic field, and a_0, a_1, and κ are coupling constants. The resulting system of equations consists of the evolution equations,

$$\nabla_a\nabla^a\phi = -\frac{a_1}{a_0}\kappa e^{-2\kappa\phi}F_{ab}F^{ab} \quad (2)$$

$$\nabla_a(e^{-2\kappa\phi}F^{ab}) = 0, \quad (3)$$

and the constraints,

$$\nabla_{[a}F_{bc]} = 0. \quad (4)$$

Consistent with Ref. [2], we choose $a_0 = 1/2$ and $a_1 = 1/4$. Adopting Cartesian coordinates, we define $\Pi \equiv \frac{\partial\phi}{\partial t}$ so that we can reexpress the evolution equations in first-order differential form as

$$E_{x,t} = B_{z,y} - B_{y,z} + 2\kappa(\Pi E_x - \phi_{,y}B_z + \phi_{,z}B_y) \quad (5)$$

$$E_{y,t} = B_{x,z} - B_{z,x} + 2\kappa(\Pi E_y + \phi_{,x}B_z - \phi_{,z}B_x) \quad (6)$$

$$E_{z,t} = B_{y,x} - B_{x,y} + 2\kappa(\Pi E_z - \phi_{,x}B_y + \phi_{,y}B_x) \quad (7)$$

$$B_{x,t} = E_{y,z} - E_{z,y} \tag{8}$$

$$B_{y,t} = E_{z,x} - E_{x,z} \tag{9}$$

$$B_{z,t} = E_{x,y} - E_{y,x} \tag{10}$$

$$\phi_{,t} = \Pi \tag{11}$$

$$\begin{aligned} \Pi_{,t} = {}& \phi_{,xx} + \phi_{,yy} + \phi_{,zz} + \kappa e^{-2\kappa\phi} \\ & \times [B_x{}^2 + B_y{}^2 + B_z{}^2 - E_x{}^2 - E_y{}^2 - E_z{}^2]. \end{aligned} \tag{12}$$

Commas within a subscript indicate partial derivatives with respect to the subsequent coordinate so that $\phi_{,y}$ is equivalent to $\partial\phi/\partial y$.

We can compute the energy as an integral over the space of the energy density ρ,

$$\rho = \rho_\phi + \rho_E + \rho_B, \tag{13}$$

where the contributions have been separated individually as

$$\rho_\phi = \frac{1}{2}(\Pi^2 + \phi_{,x}^2 + \phi_{,y}^2 + \phi_{,z}^2)$$

$$\rho_E = \frac{e^{-2\kappa\phi}}{2}(E_x^2 + E_y^2 + E_z^2)$$

$$\rho_B = \frac{e^{-2\kappa\phi}}{2}(B_x^2 + B_y^2 + B_z^2). \tag{14}$$

The dilaton differentiates this model from electrovacuum and provides for the conserved charge,

$$Q = \frac{\kappa}{2\pi}\int dx\, dy\, dz[\phi_{,x}E_x + \phi_{,y}E_y + \phi_{,z}E_z]. \tag{15}$$

Initial data must be solutions of the two constraint equations,

$$0 = (e^{-2\kappa\phi}E_x)_{,x} + (e^{-2\kappa\phi}E_y)_{,y} + (e^{-2\kappa\phi}E_z)_{,z} \tag{16}$$

$$0 = B_{x,x} + B_{y,y} + B_{z,z}. \tag{17}$$

The evolution equations preserve the constraints in the sense that the solution at a given time generated from integrating the evolution equations will also solve the constraint equations. However, numerically any deviations from the constraints could in principle grow. This is called a *free evolution* and contrasts with a *constrained evolution* in which the constraints equations are used in place of an equal number of evolution equations. As such, we can monitor the constraint *residual* which is an absolute, but generally arbitrary, measure of the extent to which the solution at a given time fails to solve the constraint equations. Numerical data presented below suggests that residuals do not grow significantly for the time scales considered here. It should be noted that methods from the
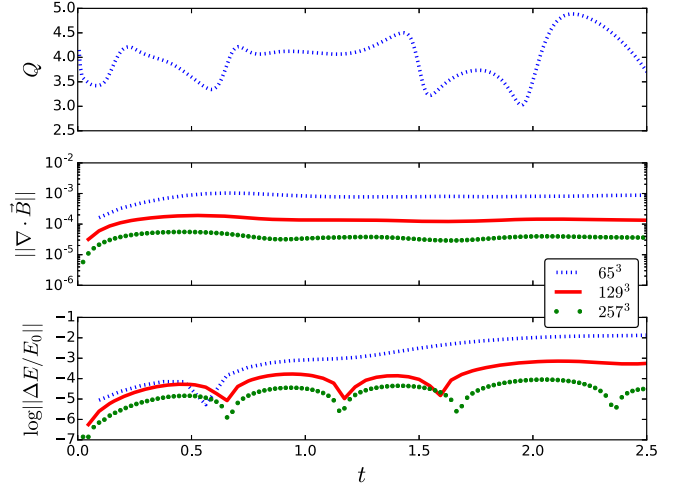

FIG. 1. Demonstration of convergence for the Gaussian initial data in Eqs. (18)–(20) with five levels of FMR refinement. (top:) The convergence order is computed over just the finest level and demonstrates convergence of the x-component of $\vec{B}$. (middle:) The norm of the divergence of the magnetic field decreases with resolution. (bottom:) The fractional energy change similarly decreases with resolution. All these indications suggest that the code is convergent and consistent.

field of computational magnetohydrodynamics such as a *divergence cleaning* or *constrained transport* could be used to control such growth.

We study the evolution of different initial data and describe that data in the following sections describing the results. The constant κ is equivalent to the α_0 of Ref. [4], and the results below adopt $\kappa = 1$ (see Ref. [2] for a discussion explaining why a change to its numerical value has no physical significance).

III. IMPLEMENTATION

We solve these equations using the distributive, adaptive mesh infrastructure for finite differences HAD [20]. We use fourth-order accurate, center differences in a method of lines scheme with a third-order accurate Runge-Kutta time integrator. We use Kreiss-Oliger-like dissipation but with high order derivatives as a mild low-pass filter to mitigate noise, as is fairly common in numerical relativity codes.

We present the results of a particular numerical test in Fig. 1. For these tests, we evolve what we call Gaussian initial data which is smooth everywhere and satisfies the constraints. Here, we set $\phi = 0 = \vec{B}$, and

$$E_x = 0 \tag{18}$$

$$E_y = \left(\frac{z}{\delta_z^2}\right)Ae^{-x^2/\delta_x^2}e^{-y^2/\delta_y^2}e^{-z^2/\delta_z^2} \tag{19}$$

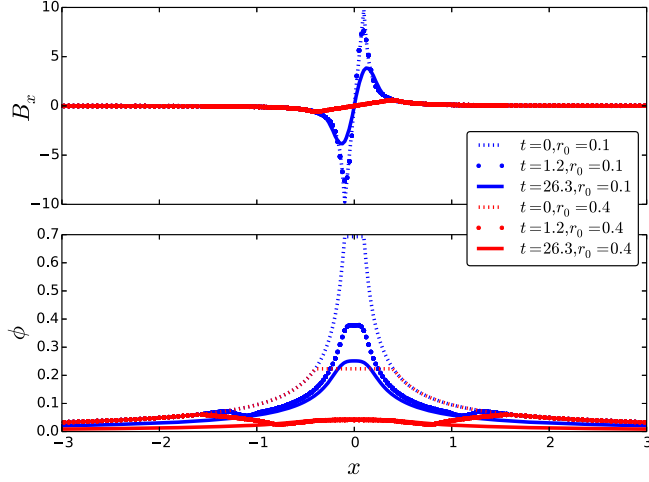$$E_z = -\left(\frac{y}{\delta_y^2}\right)Ae^{-x^2/\delta_x^2}e^{-y^2/\delta_y^2}e^{-z^2/\delta_z^2} \tag{20}$$

FIG. 2. Dynamics of the magnetic monopole. Shown are snapshots of the x-component of the magnetic field and the dilaton on the x-axis for a magnetic monopole with $P = 0.1$ and radial cutoff r_0 equal to either 0.1 or 0.4. The magnetic field settles more quickly than the dilaton which "sheds" some excess field, but the overall solution settles quickly to a stationary solution that depends on r_0.

for real parameters A, $\delta_{x|y|z}$. In the figure, we compare three different resolutions and demonstrate that the convergence order is consistent with third order. Note that these evolutions use fixed mesh refinement (FMR) and the order is computed only by comparing the finest levels. Also shown are the total divergence of the magnetic field and change in total energy versus time. Both of these represent errors and that the measures of error decrease with increasing resolution represents a test of consistency for the numerical solution.

IV. RESULTS

A. Monopoles

Another description of initial data are the monopoles of Ref. [2]. The *magnetic monopole* can be expressed in terms of a monopole charge P such that

$$\phi = \left(\frac{1}{\kappa}\right) \ln\left[P\kappa\left(\frac{1}{r} + \frac{1}{P\kappa}\right)\right] \qquad (21)$$

$$B_r = \frac{P\kappa}{r^2}. \qquad (22)$$

Because the monopole is singular at the origin, a cutoff r_0 is instituted such that for $r \leq r_0$, the radius used in the above equations is instead r_0 so that near the origin, for example, $B_x = P\kappa x/r_0^3$.

The dynamics observed for magnetic monopoles is demonstrated in Fig. 2. The magnetic monopole appears stable for all charges tried. The effect of the cutoff appears to be that the solution "sees" a charge that depends on the
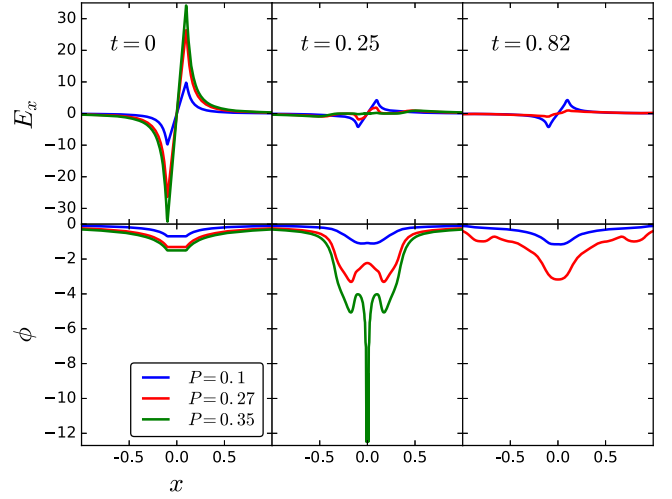

FIG. 3. Three regimes of dynamics for the electric monopole. The solution at three different times is shown for three different charges. For small charges, the monopole appears dynamically stable (see the $P = 0.1$ case shown in blue). For large charges, the dilaton grows at the center until the code no longer resolves the solution (see the $P = 0.35$ case shown in green). Instead of a sharp transition, there appears to be a regime in which the dilaton grows but saturates or otherwise stops growing (see the $P = 0.27$ case shown in red). Here the cutoff value, r_0, is equal to 0.1 and note that the spatial extent of the simulation extends much further than what is shown.

cutoff. In particular, the dilaton settles into different solutions dependent on r_0. A small value of r_0 demands a higher resolution to capture the gradients, particularly in the magnetic field (as opposed to the dilaton).

We can define an *electric monopole* similarly,

$$\phi = -\left(\frac{1}{\kappa}\right) \ln\left[P\kappa\left(\frac{1}{r} + \frac{1}{P\kappa}\right)\right] \qquad (23)$$

$$E_r = \frac{P\kappa}{r^2}. \qquad (24)$$

Again, P is the monopole charge and r_0 is the length scale at which the solution is cutoff. Three representative evolutions are shown in Fig. 3. For a small monopole charge, the solution appears stable, similar to the magnetic case. For large monopole charge, however, the solution appears unstable with the dilaton becoming more and more negative in time.

One may expect critical behavior to appear in between these two regimes as has been observed in gravitational scalar collapse [13] and in certain nongravitating nonlinear theories [14–19]. However, instead there appears to be a third regime intermediate between small and large charge in which the dilaton becomes more negative at early times and then saturates.
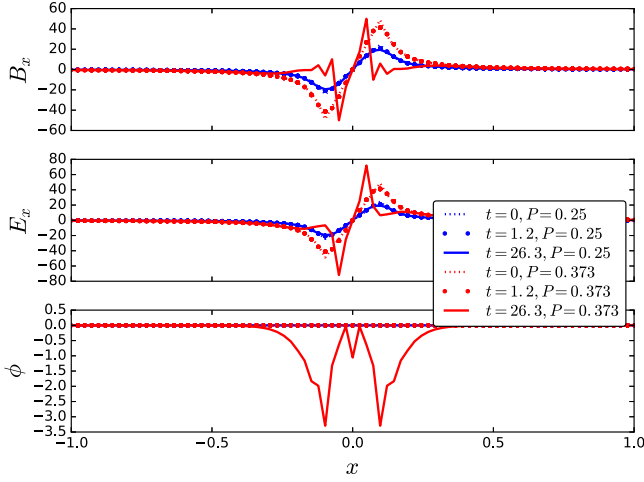
FIG. 4. Demonstration of instability in the dyonic monopole. The solution at a few different times is shown for two charges, $P = 0.25$ (stable) and $P = 0.373$ (unstable).
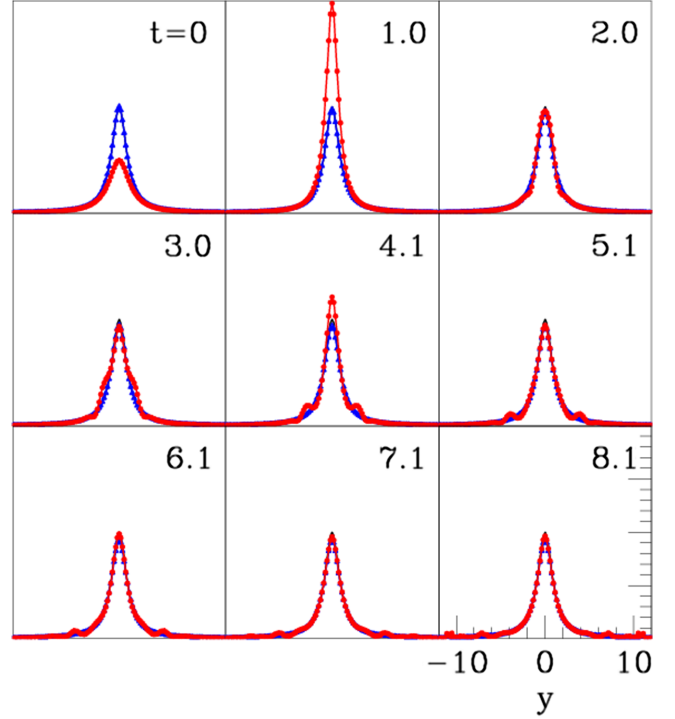

FIG. 5. Evolutions of a perturbed (blue circles) and an unperturbed (red triangles) flux tube. Shown are 1D slices of the energy density ρ at the times indicated for $x = 0 = z$. Also shown is the known, static solution (black solid line) although it is hardly visible because the other solutions overlay it. The unperturbed solution remains quite close to the static solution for the duration of the evolution. The wiggly flux tube oscillates around the static solution with the oscillation damped quickly by outgoing radiation visible in the frames $t = 3.0$ and $t = 4.1$. Noisy boundary effects are becoming apparent in the last frame. Here $H = 1$ and $a = 1$ for both solutions, and the perturbation is described by parameters: $A = 1$, $k = 2\pi/5$, and $\delta = 4$.

Likewise, we define a *dyonic monopole* as

$$\phi = 0 \tag{25}$$

$$B_r = \frac{P\kappa}{r^2} \tag{26}$$

$$E_r = \frac{P\kappa}{r^2}. \tag{27}$$

Here P is both the electric and magnetic monopole charge and r_0 is the length scale at which the solution is cutoff. Because we consider here only dyonic monopoles with equal electric and magnetic charges, the natural choice is for the dilaton to vanish.

The dynamics of these monopoles is represented in Fig. 4. Two regimes are observed depending on the charge P. For a small charge, the solution appears stable whereas for large charge, the evolution indicates instability. In particular, the dilaton becomes more and more negative while the electric field grows larger than the magnetic field. Both these behaviors suggest that the instability found for electric monopoles dominates the dynamics in this regime.

B. Flux tubes

Another type of solution, namely the flux tube as discussed in Refs. [1,2], describes a "string" of confined magnetic flux. Here, we consider the dynamics and stability of such tubes with generalized initial data given by

$$f(z) = Ae^{-z^2/\delta^2} \tag{28}$$

$$\bar{\rho} = \sqrt{(x + f \cos kz)^2 + (y + f \sin kz)^2} \tag{29}$$

$$\phi = \frac{1}{2\kappa} \log\left[\frac{4a^2}{\kappa^2 H^2 (1 + a^2\bar{\rho}^2)^2}\right] \tag{30}$$

$$B_z = He^{2\kappa\phi}. \tag{31}$$

Here, the real function $f(z)$ serves to introduce a wiggle with a wave number k, amplitude A, and width δ to the original flux tube described by real constants a and H where H describes the magnetic strength of the tube. For the parameter $A = 0$, one has a vertically oriented flux tube.

The dynamics of certain solutions are shown in Fig. 5. An unperturbed, straight tube appears stable. Note that the tube necessarily hits the boundaries of the computational domain, and thus stability is suspected based on short evolutions before boundary effects become significant throughout the domain. Likewise, for nonvanishing A, the "wiggled" string also appears stable with the perturbation quickly propagating away, leaving what appears to be the unperturbed, stationary string.

C. Evidence for singularity formation

Our final comment concerns whether this model permits singularity formation or whether the large growth observed
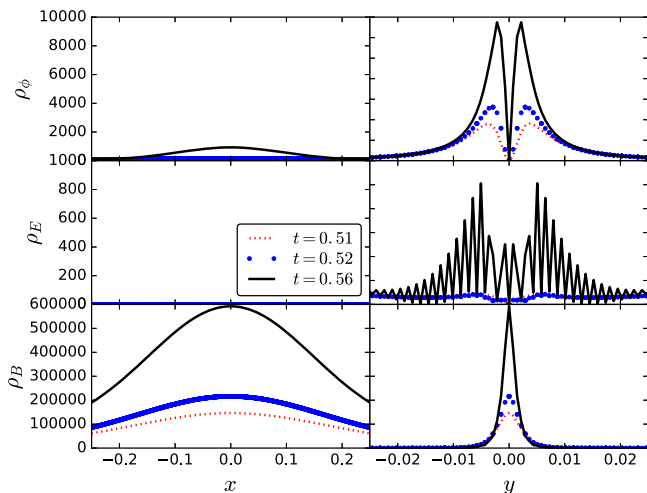
FIG. 6.   Evolution of initial data of the form found in Eqs. (18)–(20) towards apparent singularity. Slices along the x- and y- axes of the different contributions to the energy density for a particular evolution with Gaussian initial data. The energy concentrates along the x-axis, shrinking to roughly a line with thickness of order the grid spacing. Note: (i) the much smaller spatial bounds of the right column of plots versus the left, and (ii) a plot over z- would be similar to that of y-. Increasing the number of AMR levels resolves the concentration of energy better and delays slightly the point at which the code cannot handle the large gradients. That increasing resolution demonstrates this same concentration is suggestive of singularity formation. Shown is the highest resolution case with seven levels of AMR.

in the previously mentioned unstable cases ultimately saturates. Numerics likely cannot fully answer this question of global existence, but it can suggest an answer. And so instead of considering initial data which itself needs to be regularized, such as the introduction of a cutoff scale r_0 with the monopoles, we instead return to the initial data found in Eqs. (18)–(20) and for which convergence was demonstrated in Fig. 1. This initial data are smooth everywhere.

We characterize the dynamics in Fig. 6 for large amplitude by showing snapshots of the various contributions to the energy density as defined in Eq. (14). The initial data quickly evolves such that the energy concentrates along the x-axis. The adaptivity places refined grids in this vicinity. However, runs with increasing number of allowed levels of adaptive mesh refinement (AMR) all show dynamics in which the concentration reaches the grid resolution. This behavior suggests that the concentration occurs without limit, but of course such an extrapolation is a guess because the continuum equations could dictate saturation at a scale beyond the reach of these runs.

V. CONCLUSION

Numerical evolutions of various forms of initial data in the Maxwell-dilaton system indicate various regimes of stability and instability. In particular, an instability for certain electric dominated scenarios seen in the gravitating case appears to carryover to this flatspace model [4].

A particular case which demonstrated unstable growth was studied with increasing adaptive refinement that was unable to fully resolve the growth. This behavior was suggestive that the growth is unbounded and will ultimately form a singularity, although the numerics here cannot be conclusive.

Certain systems that demonstrate two disparate dynamical regimes such as singularity formation and stationarity or singularity versus dispersion have also demonstrated critical behavior at the threshold similar to black hole critical behavior [13]. However, no such behavior is found in this model.

[1] J. R. Morris, Generalized dilaton-Maxwell cosmic string and wall solutions, Phys. Lett. B **641,** 1 (2006).

[2] G. W. Gibbons and C. G. Wells, Flux confinement in dilatonic cosmic strings, Classical Quantum Gravity **11,** 2499 (1994).

[3] P. Bizon, Saddle point solutions in Yang-Mills dilaton theory, Phys. Rev. D **47,** 1656 (1993).

[4] E. W. Hirschmann, L. Lehner, S. L. Liebling, and C. Palenzuela, Black hole dynamics in Einstein-Maxwell-dilaton theory, Phys. Rev. D **97,** 064032 (2018).

[5] J. V. Rocha and M. Tomašević, Self-similarity in Einstein-Maxwell-dilaton theories and critical collapse, Phys. Rev. D **98,** 104063 (2018).

[6] M. Khalil, N. Sennett, J. Steinhoff, J. Vines, and A. Buonanno, Hairy binary black holes in Einstein-Maxwell-dilaton theory and their effective-one-body description, Phys. Rev. D **98,** 104010 (2018).

[7] R. Brito and C. Pacilio, Quasinormal modes of weakly charged Einstein-Maxwell-dilaton black holes, Phys. Rev. D **98,** 104042 (2018).

[8] C. Pacilio, Scalar charge of black holes in Einstein-Maxwell-dilaton theory, Phys. Rev. D **98**, 064055 (2018).

[9] F. Mccarthy, D. Kubizňák, and R. B. Mann, Dilatonic imprints on exact gravitational wave signatures, Phys. Rev. D **97**, 104025 (2018).

[10] F.-L. Julié, On the motion of hairy black holes in Einstein-Maxwell-dilaton theories, J. Cosmol. Astropart. Phys. 01 (2018) 026.

[11] F.-L. Julié, Reducing the two-body problem in scalar-tensor theories to the motion of a test particle: A scalar-tensor effective-one-body approach, Phys. Rev. D **97**, 024047 (2018).

[12] P. Jai-akson, A. Chatrabhuti, O. Evnin, and L. Lehner, Black hole merger estimates in Einstein-Maxwell and Einstein-Maxwell-dilaton gravity, Phys. Rev. D **96**, 044031 (2017).

[13] M. W. Choptuik, Universality and Scaling in Gravitational Collapse of a Massless Scalar Field, Phys. Rev. Lett. **70**, 9 (1993).

[14] S. L. Liebling, E. W. Hirschmann, and J. Isenberg, Critical phenomena in nonlinear sigma models, J. Math. Phys. (N.Y.) **41**, 5691 (2000).

[15] S. L. Liebling, Black hole critical phenomena without black holes, Pramana **55**, 497 (2000).

[16] S. L. Liebling, The singularity threshold of the nonlinear sigma model using 3-D adaptive mesh refinement, Phys. Rev. D **66** (2002) 041703.

[17] S. L. Liebling, The Nonlinear sigma model with distributed adaptive mesh refinement, Classical Quantum Gravity **21**, 3995 (2004).

[18] S. L. Liebling, Threshold of singularity formation in the semilinear wave equation, Phys. Rev. D **71**, 044019 (2005).

[19] S. L. Liebling, Nonlinear collapse in the semilinear wave equation in AdS space, Phys. Rev. D **87**, 081501 (2013).

[20] HAD home page, http://had.liu.edu (2010).